

Emergent Weyl-like points in periodically modulated systems and Floquet engineering

Fang Qin^{1,*} and Rui Chen^{2,†}

¹*School of Science, Jiangsu University of Science and Technology, Zhenjiang 212100, China*

²*Department of Physics, Hubei University, Wuhan 430062, China*

We investigate a three-dimensional topological phase resembling a Weyl semimetal, modulated by a periodic potential and engineered through Floquet dynamics. This system is constructed by stacking two-dimensional Chern insulators and hosts Weyl-like points defined in the parameter space (k_x, k_y, z) , distinct from conventional Weyl points in momentum space (k_x, k_y, k_z) . The Weyl-semimetal-like phase exhibits characteristics akin to those of Weyl semimetals, including linear dispersion near the Weyl-like points, nontrivial bulk topology, and the presence of Fermi arcs connecting the Weyl-like points. Unlike traditional Weyl semimetals, these features manifest in real space rather than momentum space. Additionally, we compute the layer-resolved Floquet Hall conductivity and demonstrate that the positions of the Weyl-like points can be controlled via high-frequency laser pumping.

I. INTRODUCTION

Stacks of two-dimensional (2D) Chern insulator phases have proven to be a versatile platform for realizing extraordinary topological phases, attracting considerable attention in recent years [1–20]. For instance, the well-known Weyl semimetal phase can be interpreted as a stack of 2D Chern insulators with orbital-dependent interlayer tunneling [21–25]. Similarly, phases such as the axion insulator and the hinged quantum spin Hall effect arise from alternating stacks of Chern insulators with opposite Chern numbers [26–29]. Moreover, higher-Chern-number quantum anomalous Hall insulators can be constructed by alternating stacks of Chern insulators and normal insulators [30–33].

Weyl semimetals are characterized by linearly dispersing band-touching points, known as Weyl points, in momentum space [34–37]. These Weyl points are topologically protected and act as monopoles or antimonopoles of the Berry curvature [38, 39]. According to the no-go theorem [40, 41], Weyl points always appear in pairs and are connected by surface states known as Fermi arcs.

Recent advancements have realized ideal Weyl semimetals across various platforms. They have been implemented in electrical circuits [42, 43], ultracold atomic gases with three-dimensional (3D) spin-orbit coupling [44–47], photonic crystals [48, 49], and acoustic metamaterials [50–52].

Zhang *et al.* recently proposed and studied a 2D phase modulated by a periodic potential [53]. This system exhibits edge modes with spectral flow dependent on position, in contrast to traditional Chern insulators, where the spectral flow of edge modes depends on momentum. Moreover, they suggested that the periodic potential could be experimentally realized through the effects of charge density waves [54, 55].

In this work, we propose and study a 3D topological phase resembling a Weyl semimetal, modulated by a periodic potential and realized through a simple stack of 2D Chern insulators. The system features Weyl-like points defined in the parameter space (k_x, k_y, z) , distinct from the conventional Weyl points in momentum space (k_x, k_y, k_z) . This Weyl-semimetal-like phase exhibits key properties of a Weyl semimetal, including linear dispersion near the Weyl-like points, nontrivial bulk topology, and the emergence of Fermi arcs connecting these points. However, these behaviors are observed in real space, rather than momentum space, as in traditional Weyl semimetals. Additionally, we calculate the layer-resolved Floquet Hall conductivity under high-frequency periodic driving and show that the positions of the Weyl-semimetal-like nodes can be tuned by high-frequency laser driving.

The structure of this paper is as follows: In Section II, we introduce the Weyl-like lattice Hamiltonian with a periodic potential along the z -direction, along with the conventional Weyl semimetal model, and discuss the duality between these two models. In Section III, we derive the Floquet effective Hamiltonians for both models under high-frequency laser pumping. Section IV presents calculations of the Floquet Weyl nodes, the layer Floquet Chern number, the Floquet energy spectrum, and the Floquet Fermi arc for both models under high-frequency laser driving. A brief discussion on potential experimental realizations of the Weyl-like model is provided in Section V. Finally, Section VI offers a summary of the key results.

II. MODEL

We begin with the two-band model Hamiltonian describing a stack of 2D Chern insulators in a periodic potential along the z -direction,

$$H = \sum_{j_z} [h_{2D} + V(z)\sigma_z] c_{j_z}^\dagger c_{j_z}, \quad (1)$$

* qinfang@just.edu.cn

† chenr@hubei.edu.cn

where $c_{j_z}^\dagger$ is the electron creation operator in the j_z -th layer, $h_{2D} = m_z \sigma_z + m_0 [2 - \cos(k_x a) - \cos(k_y a)] \sigma_z + t_x \sin(k_x a) \sigma_x + t_y \sin(k_y a) \sigma_y$ represents the Chern insulator Hamiltonian when $m_z \times m_0 < 0$. Here, a is the lattice constant, and σ_i ($i = x, y, z$) are Pauli matrices acting on the orbital space. The spatially periodic potential is given by $V(z) = V_z \cos(Q_z z)$, where V_z is the potential strength, $z = j_z a$ is the position along the z -direction, and $\lambda_z = 2\pi/Q_z$ is the periodic wavelength. In the following calculations, we use the fixed parameters $m_z = 0.5$ eV, $m_0 = 1$ eV, $t_x = t_y = t_0 = 1$ eV, $V_z = 1$ eV, and $\lambda_z = 31a$ with $a = 1$ nm. The detailed derivation of the matrix form for the real-space model in a periodic potential along the z -direction, with open boundary conditions (OBCs) in y -direction and periodic boundary conditions (PBCs) in x -direction, is provided in Section SI in the Supplemental Material [56].

A. Weyl-like model

The spectral flow of the system is described by the Weyl-like model Hamiltonian density, Eq. (1), defined in the (k_x, k_y, z) -space as follows:

$$\mathcal{H} = [m_z + V_z \cos(Q_z z)] \sigma_z + m_0 [2 - \cos(k_x a) - \cos(k_y a)] \sigma_z + t_x \sin(k_x a) \sigma_x + t_y \sin(k_y a) \sigma_y. \quad (2)$$

As shown in Fig. 1(a1), the system can be interpreted as an array of isolated 2D systems, each with a different topological mass: $\tilde{m}_z(z) = m_z + V(z)$, where $V(z) = V_z \cos(Q_z z)$.

To study the topological properties of the system, we define the layer-resolved Chern number for the m -th occupied band as [6, 14, 27, 57–66]

$$C_m(z) = \frac{1}{2\pi} \int \mathcal{F}_{xy}^{mm}(\mathbf{k}, z) d^2 \mathbf{k}, \quad (3)$$

where the non-Abelian Berry curvature is given by [6, 64–66]

$$\mathcal{F}_{xy}^{mn}(\mathbf{k}, z) = \partial_{k_x} \mathcal{A}_{k_y}^{mn}(\mathbf{k}, z) - \partial_{k_y} \mathcal{A}_{k_x}^{mn}(\mathbf{k}, z) + i[\mathcal{A}_{k_x}^{mn}(\mathbf{k}, z), \mathcal{A}_{k_y}^{mn}(\mathbf{k}, z)], \quad (4)$$

where $\mathcal{A}_{k_\alpha}^{mn}(\mathbf{k}, z)$ is the Berry connection of the occupied bands with $m, n \in \text{occ}$, defined as

$$\mathcal{A}_{k_\alpha}^{mn}(\mathbf{k}, z) = i \langle \psi_m | \partial_{k_\alpha} \psi_n \rangle. \quad (5)$$

Here, “occ” is used to denote the occupied bands. A detailed derivation of the non-Abelian Berry curvature in (4) is provided in Section SII in the Supplemental Material [56].

The layer-resolved Chern number is illustrated in Fig. 1(c1). Figures 1(a1) and 1(b1) show that each 2D system behaves as a Chern insulator with a Chern number $|C| = 1$ for $z_{c-} < z < z_{c+}$, and as a normal insulator with $C = 0$ for $z < z_{c-}$ and $z > z_{c+}$. The critical values

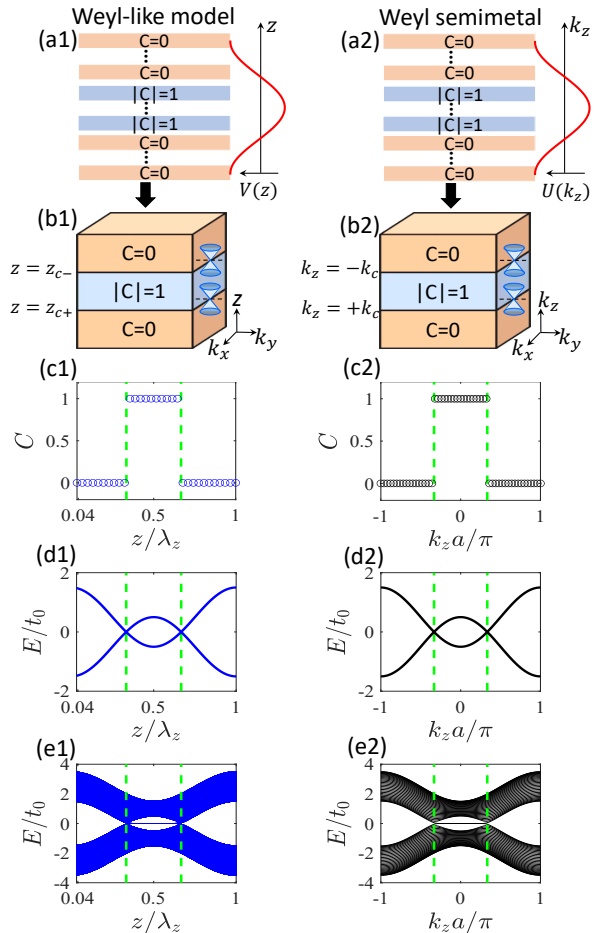


FIG. 1. Duality between the decoupled Weyl-like model (left column) and the Weyl semimetal model (right column). (a1) Schematic representation of the decoupled Weyl-like model in real space, featuring a spatially periodic potential $V(z) = V_z \cos(Q_z z)$, where $Q_z = 2\pi/\lambda_z$. (b1) Weyl cones in (k_x, k_y, z) space at two critical planes, (k_x, k_y, z_{c-}) and (k_x, k_y, z_{c+}) , marking topological transitions. (c1) Layer-resolved Chern number as a function of layer z for the decoupled Weyl-like model with $V_z = 1$ eV, $\lambda_z = L_z = 31a$, and the lattice constant $a = 1$ nm. (d1) Energy spectrum (blue solid curves) for the Weyl-like model with $k_x = k_y = 0$. (e1) Energy spectrum (blue solid curves) and Fermi-like arc (blue horizontal line for $E = 0$) for the Weyl-like model under OBCs along the y -direction, with $k_x = 0$ and system size $L_y = 31a$. (a2) Schematic representation of the Weyl semimetal model in real space, with a momentum-periodic potential $U(k_z) = t_z \cos(k_z a)$. (b2) Weyl cones in the (k_x, k_y, k_z) momentum space at two critical planes $(k_x, k_y, -k_c)$ and $(k_x, k_y, +k_c)$, indicating the topological features of the model. (c2) Chern number as a function of momentum k_z for the Weyl semimetal model with $t_z = 1$ eV. (d2) Energy spectrum (black solid curves) for the Weyl semimetal model with $k_x = k_y = 0$. (e2) Energy spectrum (black solid curves) and Fermi arc (black horizontal line for $E = 0$) for the Weyl semimetal model under OBCs along the y -direction, with $k_x = 0$ and system size $L_y = 31a$. The other parameters are $m_z = 0.5$ eV, $m_0 = 1$ eV, $t_x = t_y = t_0 = 1$ eV, and $L_z = 31a$.

of z , denoted by $z_{c\pm}$, are determined by the condition $\tilde{m}_z(z) = m_z + V(z) = 0$ and are given by:

$$\frac{z_{c\pm}}{\lambda_z} = \frac{1}{2\pi} \left[\pi \pm \arccos \left(\frac{m_z}{V_z} \right) \right], \quad (6)$$

where the condition $-1 \leq \tilde{m}_z/V_z \leq 1$ is satisfied.

Figure 1(d1) shows the energy spectrum as a function of position z with $k_x = k_y = 0$. Notably, a band inversion is observed near $z = z_{c\pm}$, clearly illustrating the spectral flow of the stacked system. Additionally, the edge states (zero-energy modes) can be observed in Fig. 1(e1) that are dual to Fig. 1(e2).

B. Weyl semimetal

To facilitate a comparative study, we review the Weyl semimetal model Hamiltonian, which takes the following form [21–24]

$$\begin{aligned} \mathcal{H}_W(\mathbf{k}) = & [-m_z + t_z \cos(k_z a)] \sigma_z \\ & - m_0 [2 - \cos(k_x a) - \cos(k_y a)] \sigma_z \\ & + t_x \sin(k_x a) \sigma_x + t_y \sin(k_y a) \sigma_y, \end{aligned} \quad (7)$$

where the Hamiltonian describes the Weyl semimetal phase, which can be interpreted as a stack of 2D materials with orbital-dependent hopping t_z , as illustrated in Fig. 1(a2). The matrix form of this Hamiltonian (7) in real space, with OBCs in the z -direction and PBCs in the x - and y -directions, is provided in Subsection SIII A in the Supplemental Material [56]. Similarly, the matrix form with OBCs in the y -direction and PBCs in the x - and z -directions is given in Subsection SIII B in the Supplemental Material [56].

Rewriting Eq. (7) in the form $\mathcal{H}_W(\mathbf{k}) = \mathbf{h}(\mathbf{k}) \cdot \boldsymbol{\sigma}$, where $\mathbf{h}(\mathbf{k}) = (h_x, h_y, h_z)$, we define the components as: $h_x = t_x \sin(k_x a)$, $h_y = t_y \sin(k_y a)$, $h_z = M_z(k_z) - m_0 [2 - \cos(k_x a) - \cos(k_y a)]$, with $M_z(k_z) = -m_z + t_z \cos(k_z a)$. The eigenenergies of this 2D model Hamiltonian (7) are given by

$$E_{W,\pm} = \pm \sqrt{h_x^2 + h_y^2 + h_z^2}. \quad (8)$$

Thus, the energy gap between the top and bottom surfaces at $k_x = k_y = 0$ is: $\Delta_W = E_{W,+} - E_{W,-} = 2|M_z(k_z)|$ as shown in Fig. 1(d2).

The Chern number of the Weyl semimetal model (7) can then be calculated using the expression [9, 10, 19, 57, 67–69]

$$C(k_z) = \frac{1}{4\pi} \int_{\text{B.Z.}} d^2\mathbf{k} \frac{\mathbf{h}(\mathbf{k})}{|\mathbf{h}(\mathbf{k})|^3} \cdot [\partial_{k_x} \mathbf{h}(\mathbf{k}) \times \partial_{k_y} \mathbf{h}(\mathbf{k})], \quad (9)$$

where $\mathbf{k} = (k_x, k_y)$ and the integral is over the 2D Brillouin zone. A detailed analytical expression for the Chern number (9) of the Weyl semimetal model (7) is provided in Section SIV in the Supplemental Material [56].

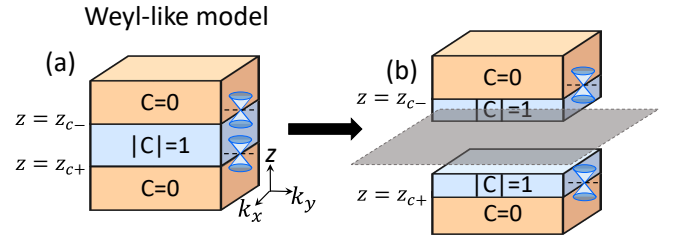


FIG. 2. (a) Weyl-like nodes at $z = z_{c-}$ and $z = z_{c+}$, marking topological transitions. (b) The two Weyl-like nodes are separated by the bulk gap between $z = z_{c-}$ and $z = z_{c+}$. Each half of the system contains a single Weyl-like node. This differs from conventional Weyl points, which typically appear in pairs in momentum space (k_x, k_y, k_z) .

For the special case where $k_x = k_y = 0$, the eigenenergies of the Weyl semimetal Hamiltonian (7) are:

$$E_{\pm} = \pm [-m_z + t_z \cos(k_z a)]. \quad (10)$$

In this case, the system hosts a pair of gapless Weyl nodes at $(0, 0, k_{c\pm})$ with the positions $k_{c\pm} = \pm \frac{1}{a} \arccos(m_z/t_z)$, under the condition $|m_z/t_z| \leq 1$ as shown in Figs. 1(b2) and 1(c2). These Weyl nodes k_c are obtained by solving $M_z(k_z) = -m_z + t_z \cos(k_z a) = 0$ with the condition $-1 \leq m_z/t_z \leq 1$. For k_z values within the range $k_{c-} < k_z < k_{c+}$, the system behaves as a Chern insulator with Chern number $C = 1$. Outside this range, for $k_z < k_{c-}$ or $k_z > k_{c+}$, the system becomes a normal insulator with $C = 0$, as depicted in Fig. 1(c2).

C. Comparison between the two models

As shown in Fig. 1, the two models – the decoupled Weyl-like model (left column) and the Weyl semimetal model (right column) – can be viewed as duals of each other. The Weyl-like model in Eq. (2) provides a generic framework for describing Weyl semimetals, including key features such as band touching, Chern number, and Fermi arcs, all of which are captured by the Weyl semimetal model in Eq. (7). Figure 2 illustrates that the two Weyl-like nodes are separated by the bulk gap between $z = z_{c-}$ and $z = z_{c+}$, with each half of the system hosting a single Weyl-like node. This contrasts with conventional Weyl points, which, due to the no-go theorem [40, 41], typically appear in pairs in momentum space with opposite chiralities. Below, we will focus on the case involving Floquet engineering.

III. FLOQUET HAMILTONIAN

To investigate the Floquet engineering of the two models discussed in Section II, we derive their effective Floquet Hamiltonians.

The optical field propagating along the z -direction in the material is given by $\mathbf{E}(t) = \partial \mathbf{A}(t)/\partial t =$

$E_0(\cos(\omega t), \cos(\omega t + \varphi), 0)$, where E_0 is the amplitude, ω is the angular frequency, and φ represents the phase. For linear polarization, $\varphi = 0$, while $\varphi = \mp\pi/2$ corresponds to left- or right-handed circular polarization. The vector potential is periodic with period $T = 2\pi/\omega$, and it is given by $\mathbf{A}(t) = \mathbf{A}(t + T) = \omega^{-1}E_0(\sin(\omega t), \sin(\omega t + \varphi), 0)$. In the off-resonant regime, where the central Floquet band is well-separated from other replicas, the high-frequency expansion applies. We choose the optical frequency as $\hbar\omega = 10$ eV, which is much larger than the material's bandwidth [5, 16, 17, 19, 70–75].

Under optical driving, the electron motion is modified by minimal coupling to the electromagnetic gauge field $\mathbf{A}(t)$, resulting in the photon-dressed effective Hamiltonian:

$$\mathcal{H}(\mathbf{k}, t) = \mathcal{H}\left(\mathbf{k} - \frac{e}{\hbar}\mathbf{A}(t)\right). \quad (11)$$

Next, we derive the effective Floquet Hamiltonian [76–81]

$$\mathcal{H}^{(F)}(\mathbf{k}) = \frac{i}{T} \ln \left[\mathcal{T} e^{-i \int_0^T \mathcal{H}(\mathbf{k}, t) dt} \right], \quad (12)$$

where \mathcal{T} is the time-ordering operator. In the high-frequency regime, a closed-form solution exists via the high-frequency expansion [81–89]:

$$\mathcal{H}^{(F)}(\mathbf{k}) = \mathcal{H}_0 + \sum_{n=1}^{\infty} \frac{[\mathcal{H}_{-n}, \mathcal{H}_n]}{n\hbar\omega} + \mathcal{O}(\omega^{-2}), \quad (13)$$

where $\mathcal{H}_{m-m'} = \frac{1}{T} \int_0^T \mathcal{H}(\mathbf{k}, t) e^{i(m-m')\omega t} dt$, and m, m' are integers.

A. Floquet Weyl-like model

From Eq. (13), the Floquet Hamiltonian for the Weyl-like model can be expressed as

$$\mathcal{H}^{(F)}(\mathbf{k}) = \sum_{i=x,y,z} h_i \sigma_i, \quad (14)$$

where

$$\begin{aligned} h_x &= \mathcal{J}_0(A_0 a) t_x \sin(k_x a) \\ &\quad - \sum_{n \in \text{odd}, n > 0} \frac{4t_x m_0 \mathcal{J}_n^2(A_0 a)}{n\hbar\omega} \sin(n\varphi) \sin(k_x a) \cos(k_y a), \end{aligned} \quad (15)$$

$$\begin{aligned} h_y &= \mathcal{J}_0(A_0 a) t_y \sin(k_y a) \\ &\quad - \sum_{n \in \text{odd}, n > 0} \frac{4t_x m_0 \mathcal{J}_n^2(A_0 a)}{n\hbar\omega} \sin(n\varphi) \cos(k_x a) \sin(k_y a), \end{aligned} \quad (16)$$

$$\begin{aligned} h_z &= m_z + V_z \cos(Q_z z) + 2m_0 [1 - \mathcal{J}_0(A_0 a)] \\ &\quad + \mathcal{J}_0(A_0 a) m_0 [2 - \cos(k_x a) - \cos(k_y a)] \\ &\quad + \sum_{n \in \text{odd}, n > 0} \frac{4t_x t_y \mathcal{J}_n^2(A_0 a)}{n\hbar\omega} \sin(n\varphi) \cos(k_x a) \cos(k_y a), \end{aligned} \quad (17)$$

$\mathcal{J}_n(A_0 a)$ is the n th Bessel function of the first kind [90], and $A_0 = eE_0/(\hbar\omega)$. The detailed derivations leading to Eq. (14) are provided in Subsection SV A in the Supplemental Material [56]. For $\varphi=0$ (linearly polarized laser), the Weyl-like nodes are determined by solving the equation $m_z + V_z \cos(Q_z z) + 2m_0 [1 - \mathcal{J}_0(A_0 a)] = 0$, subject to the condition $-1 \leq \cos(Q_z z) = \{m_z + 2m_0 [1 - \mathcal{J}_0(A_0 a)]\} / V_z \leq 1$. This yields the Weyl-like nodes at

$$\frac{z_{c\pm}}{\lambda_z} = \frac{1}{2\pi} [\pi \pm \arccos(\tilde{m}_z(A_0)/V_z)], \quad (18)$$

where $\tilde{m}_z(A_0) = m_z + 2m_0 [1 - \mathcal{J}_0(A_0 a)]$ and $-1 \leq \tilde{m}_z(A_0)/V_z \leq 1$. By substituting the model parameters $m_z = 0.5$ eV, $m_0 = 1$ eV, $V_z = 1$ eV, and $a = 1$ nm into the condition $|\tilde{m}_z(A_0)/V_z| < 1$, we have $A_0 < 1.034$ nm⁻¹. From Eq. (18), it is clear that the position of the Weyl-like nodes can be tuned by adjusting the intensity of the optical field.

Additionally, Section SVI of the Supplemental Material [56] presents the derivations for the Weyl-like model under PBCs along the x -direction and OBCs along the y -direction.

B. Floquet Weyl semimetal

The Floquet Hamiltonian for the Weyl semimetal, derived from Eq. (13), takes the form:

$$\mathcal{H}_W^{(F)}(\mathbf{k}) = \sum_{i=x,y,z} h_i \sigma_i, \quad (19)$$

where

$$\begin{aligned} h_x &= \mathcal{J}_0(A_0 a) t_x \sin(k_x a) \\ &\quad + \sum_{n \in \text{odd}, n > 0} \frac{4t_x m_0 \mathcal{J}_n^2(A_0 a)}{n\hbar\omega} \sin(n\varphi) \sin(k_x a) \cos(k_y a), \end{aligned} \quad (20)$$

$$\begin{aligned} h_y &= \mathcal{J}_0(A_0 a) t_y \sin(k_y a) \\ &\quad + \sum_{n \in \text{odd}, n > 0} \frac{4t_x m_0 \mathcal{J}_n^2(A_0 a)}{n\hbar\omega} \sin(n\varphi) \cos(k_x a) \sin(k_y a), \end{aligned} \quad (21)$$

$$\begin{aligned} h_z &= -m_z + t_z \cos(k_z a) - 2m_0 [1 - \mathcal{J}_0(A_0 a)] \\ &\quad - \mathcal{J}_0(A_0 a) m_0 [2 - \cos(k_x a) - \cos(k_y a)] \\ &\quad + \sum_{n \in \text{odd}, n > 0} \frac{4t_x t_y \mathcal{J}_n^2(A_0 a)}{n\hbar\omega} \sin(n\varphi) \cos(k_x a) \cos(k_y a). \end{aligned} \quad (22)$$

A detailed derivation of Eq. (19) is provided in Subsection SV B in the Supplemental Material [56]. For linearly polarized light ($\varphi=0$), the Weyl nodes are determined by solving the equation $-m_z + t_z \cos(k_z a) - 2m_0 [1 - \mathcal{J}_0(A_0 a)] = 0$, subject to the condition $-1 \leq \cos(k_z a) = \{m_z + 2m_0 [1 -$

$\mathcal{J}_0(A_0a)\}/t_z \leq 1$. This condition gives the Weyl node positions:

$$k_{c\pm} = \pm \frac{1}{a} \arccos(\tilde{m}_z(A_0)/t_z), \quad (23)$$

where $\tilde{m}_z(A_0) = m_z + 2m_0[1 - \mathcal{J}_0(A_0a)]$ and $-1 \leq \tilde{m}_z(A_0)/t_z \leq 1$. Substituting typical model parameters, $m_z = 0.5$ eV, $m_0 = 1$ eV, $t_z = 1$ eV, and $a = 1$ nm, into the condition $|\tilde{m}_z(A_0)/t_z| < 1$, we obtain the constraint $A_0 < 1.034$ nm⁻¹. From Eq. (23), we can conclude that the position of the Weyl nodes can be tuned by adjusting the intensity of the optical field.

The detailed derivation of the Floquet Hamiltonian matrix for the Weyl semimetal, under OBCs along the z -direction and PBCs along the x - and y -directions, is provided in Subsection SVII A of the Supplemental Material [56]. Similarly, Subsection SVII B of the Supplemental Material [56] presents the derivation for the case of PBCs along the x - and z -directions and OBCs along the y -direction.

C. Validity

To quantitatively assess the validity of the high-frequency expansion, we estimate the maximum instantaneous energy of the time-dependent Hamiltonian $\mathcal{H}(\mathbf{k} - \frac{e}{\hbar}\mathbf{A}(t))$ averaged over a period of the field. Specifically, we require the condition at the Γ -point ($k_x = k_y = 0$) to be satisfied: $\frac{1}{T} \int_0^T dt \max\{|\mathcal{H}(\mathbf{k}, t)|\} < \hbar\omega$. This implies that the optical field parameters must satisfy $\text{Max}(t_x A_0 a, t_y A_0 a, m_0 A_0^2 a^2) < \hbar\omega$. In the high-frequency regime, with $\hbar\omega = 100$ eV as an example, we obtain: $A_0 < \text{Min}\left(\frac{\hbar\omega}{at_x}, \frac{\hbar\omega}{at_y}, \frac{1}{a}\sqrt{\frac{\hbar\omega}{m_0}}\right)$. For the model parameters $t_x = t_y = 1$ eV and $m_0 = 1$ eV, this gives $A_0 = eE_0/(\hbar\omega) < 10$ nm⁻¹. Combining the condition $A_0 < 10$ nm⁻¹ with the constraint for the Weyl nodes $A_0 < 1.034$ nm⁻¹, we conclude that $A_0 < 1.034$ nm⁻¹. This ensures that the high-frequency expansion remains valid under the specified conditions.

IV. NUMERICAL RESULTS FOR FLOQUET ENGINEERING

In this section, we present the numerical results for Floquet engineering, with a comparative analysis between the Floquet Weyl-like and Floquet Weyl semimetal models.

A. Floquet Weyl nodes

As shown in Fig. 3, the positions of the Floquet Weyl-like nodes [Fig. 3(a)] and the Floquet Weyl nodes [Fig. 3(b)] can be controlled by the light intensity A_0 .

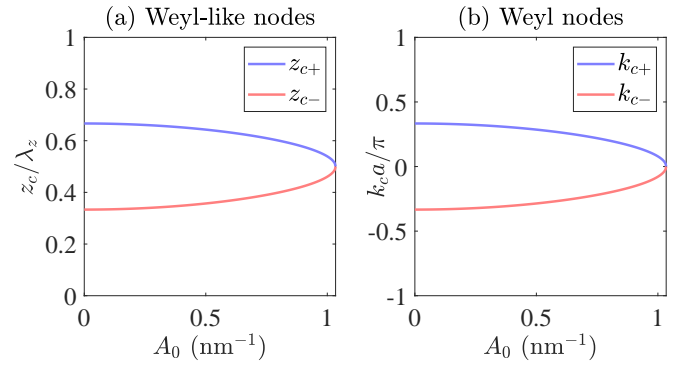


FIG. 3. (a) Floquet Weyl-like nodes and (b) Floquet Weyl nodes as a function of light intensity A_0 . The parameters are $\varphi = 0$ (linearly polarized laser), $m_z = 0.5$ eV, $m_0 = 1$ eV, $t_x = t_y = 1$ eV, $V_z = 1$ eV, $t_z = 1$ eV, and $L_z = \lambda_z = 31a$.

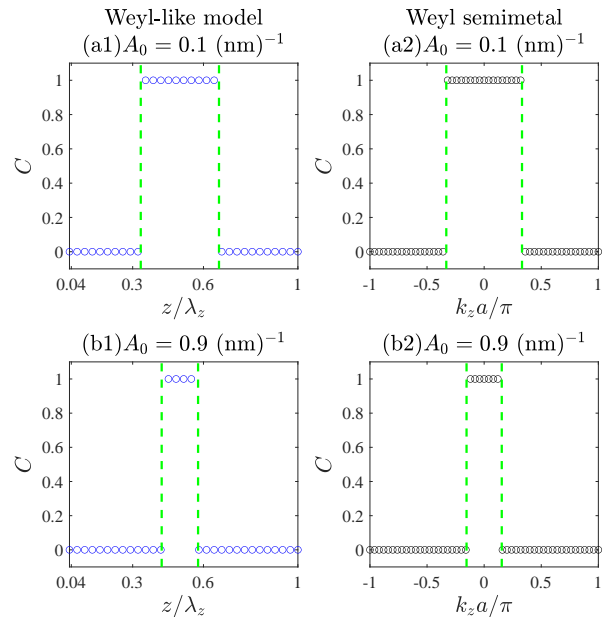


FIG. 4. Chern numbers for (a1,b1) the Floquet Weyl-like model and (a2,b2) the Floquet Weyl semimetal. (a1,a2) $A_0 = 0.1$ nm⁻¹; (b1,b2) $A_0 = 0.9$ nm⁻¹. The other parameters are the same as those in Fig. 3.

Particularly, when A_0 reaches a threshold value of approximately ~ 1.034 nm⁻¹, the two Floquet Weyl-like nodes (or Floquet Weyl nodes) merge into a single node, signaling a topological transition.

B. Floquet Chern number

We compute the Chern numbers for both the Floquet Weyl-like model and the Floquet Weyl semimetal model, as shown in Fig. 4. The results indicate that the phase transition points, represented by the Floquet Weyl nodes, shift with varying light intensities. Detailed derivations of the Chern numbers for both Floquet models are pro-

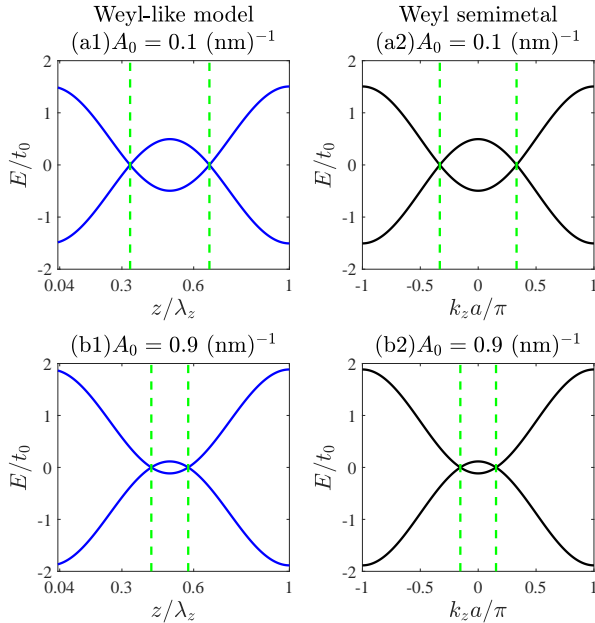


FIG. 5. Energy spectra for (a1,b1) the Floquet Weyl-like model and (a2,b2) the Floquet Weyl semimetal with $k_x = k_y = 0$. (a1,a2) $A_0 = 0.1 \text{ nm}^{-1}$; (b1,b2) $A_0 = 0.9 \text{ nm}^{-1}$. The other parameters are the same as those in Fig. 3.

vided in Sections SVIII and SIX in the Supplemental Material [56], respectively.

C. Floquet energy spectrum

The energy spectra for the Floquet Weyl-like model and the Floquet Weyl semimetal, calculated at $k_x = k_y = 0$, are shown in Fig. 5. The energy gapless points, corresponding to the Weyl nodes, exhibit a dependence on the light intensity.

D. Floquet Fermi arc

In Fig. 6, we show the energy spectra (solid curves) and Fermi arcs (depicted as horizontal straight lines at $E = 0$) for both the Floquet Weyl-like model and the Floquet Weyl semimetal under OBCs along the y -direction, with $k_x = 0$ and $L_y = 31a$. We observe that the lengths of the Floquet Fermi arcs change with light intensity, reflecting variations in the Floquet Weyl nodes.

V. EXPERIMENTAL REALIZATIONS

In this section, we discuss potential experimental realizations of the Weyl-like model. Weyl semimetals have been successfully realized in various platforms, including electrical circuits [42, 43], ultracold atomic gases [46, 47],

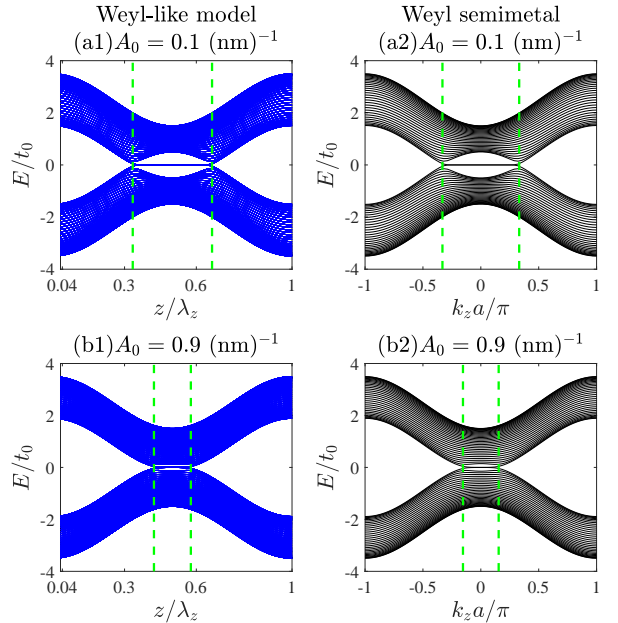


FIG. 6. Energy spectra (solid curves) and Fermi arcs (horizontal straight line for $E = 0$) for (a1,b1) the Floquet Weyl-like model and (a2,b2) the Floquet Weyl semimetal under OBCs along the y direction with $k_x = 0$ and $L_y = 31a$. (a1,a2) $A_0 = 0.1 \text{ nm}^{-1}$; (b1,b2) $A_0 = 0.9 \text{ nm}^{-1}$. The other parameters are the same as those in Fig. 3.

photonic crystals [48, 49], and acoustic metamaterials [50–52]. For the purpose of illustration, we focus on the realization of the Weyl-like model using electrical circuits.

Unlike the 3D cubic lattices employed in cold-atom proposals [44, 45] and experimental realizations [46, 47], we propose a design based on a stack of 2D square lattices, with each plaquette in every principal plane hosting a flux of π , as described in Ref. [91]. This configuration corresponds to a system of spin-1/2 particles with engineered spin-dependent tunneling.

The system thus takes the form of a multi-layer 2D time-reversal symmetric tight-binding model, with two sites per unit cell. This differs from the 3D time-reversal symmetric tight-binding model on a cubic lattice, which was originally proposed in Ref. [42] to realize Weyl semimetals in 3D momentum space.

To implement this multi-layer 2D square lattice in an electrical circuit, each lattice site is represented by an inductor, while tunnel couplings are modeled by pairs of capacitors. Zero-phase tunnel couplings connect the positive ends of adjacent inductors, while their negative ends are similarly linked. A π -phase tunnel coupling capacitively links the positive end of one inductor to the negative end of a neighboring inductor, and vice versa.

The stacking of the 2D square lattice layers is coupled with a spatially periodic potential, which can be induced by an alternating current [72] or via the charge-density-wave mechanism [53, 55]. This approach offers

a promising platform for simulating the Weyl-like model, enabling experimental exploration of its novel topological properties.

VI. SUMMARY

In our study, we introduce a novel 3D topological phase with Weyl-semimetal-like characteristics, which is induced by a periodic potential. This phase is realized by stacking 2D Chern insulators, leading to Weyl-like points in the parameter space (k_x, k_y, z) , in contrast to the conventional Weyl points in momentum space (k_x, k_y, k_z) .

The Weyl-semimetal-like phase we propose shares key features with traditional Weyl semimetals, such as linear dispersion near the Weyl-like points, nontrivial bulk topology, and the emergence of Fermi arcs that connect these points. Importantly, these topological behaviors manifest in real space, rather than in momentum space.

Additionally, our investigation explores the effects of high-frequency periodic driving, where we calculate Floquet Weyl nodes, layer Floquet Chern numbers, Floquet energy spectra, and Floquet Fermi arcs. We demonstrate that the Weyl-semimetal-like nodes can be tuned via high-frequency laser driving, providing a means to manipulate these topological features. This work opens new possibilities for exploring and controlling topological phases through external stimuli.

ACKNOWLEDGMENTS

We acknowledge helpful discussions with Ching Hua Lee. R.C. acknowledges the support from the National Natural Science Foundation of China (Grant No. 12304195) and the Chutian Scholars Program in Hubei Province.

-
- [1] Masataka Mogi, Minoru Kawamura, Atsushi Tsukazaki, Ryutaro Yoshimi, Kei S Takahashi, Masashi Kawasaki, and Yoshinori Tokura, "Tailoring tricolor structure of magnetic topological insulator for robust axion insulator," *Science advances* **3**, eaao1669 (2017).
- [2] M Mogi, M Kawamura, R Yoshimi, A Tsukazaki, Y Kozuka, N Shirakawa, KS Takahashi, M Kawasaki, and Y Tokura, "A magnetic heterostructure of topological insulators as a candidate for an axion insulator," *Nature materials* **16**, 516–521 (2017).
- [3] Di Xiao, Jue Jiang, Jae-Ho Shin, Wenbo Wang, Fei Wang, Yi-Fan Zhao, Chaoxing Liu, Weida Wu, Moses H. W. Chan, Nitin Samarth, and Cui-Zu Chang, "Realization of the axion insulator state in quantum anomalous Hall sandwich heterostructures," *Phys. Rev. Lett.* **120**, 056801 (2018).
- [4] M Mogi, Y Okamura, M Kawamura, R Yoshimi, K Yasuda, A Tsukazaki, KS Takahashi, T Morimoto, N Nagaosa, M Kawasaki, *et al.*, "Experimental signature of the parity anomaly in a semi-magnetic topological insulator," *Nature Physics* **18**, 390–394 (2022).
- [5] Fang Qin, Ching Hua Lee, and Rui Chen, "Light-induced half-quantized Hall effect and axion insulator," *Phys. Rev. B* **108**, 075435 (2023).
- [6] Rui Chen and Shun-Qing Shen, "On the half-quantized Hall conductance of massive surface electrons in magnetic topological insulator films," *Science China Physics, Mechanics & Astronomy* **67**, 1–10 (2024).
- [7] Cui-Zu Chang, Jinsong Zhang, Xiao Feng, Jie Shen, Zuo Cheng Zhang, Minghua Guo, Kang Li, Yunbo Ou, Pang Wei, Li-Li Wang, *et al.*, "Experimental observation of the quantum anomalous Hall effect in a magnetic topological insulator," *Science* **340**, 167–170 (2013).
- [8] R Yoshimi, K Yasuda, A Tsukazaki, KS Takahashi, N Nagaosa, M Kawasaki, and Y Tokura, "Quantum Hall states stabilized in semi-magnetic bilayers of topological insulators," *Nature communications* **6**, 8530 (2015).
- [9] Wen-Yu Shan, Hai-Zhou Lu, and Shun-Qing Shen, "Effective continuous model for surface states and thin films of three-dimensional topological insulators," *New Journal of Physics* **12**, 043048 (2010).
- [10] Hai-Zhou Lu, Wen-Yu Shan, Wang Yao, Qian Niu, and Shun-Qing Shen, "Massive Dirac fermions and spin physics in an ultrathin film of topological insulator," *Phys. Rev. B* **81**, 115407 (2010).
- [11] Huichao Li, L. Sheng, D. N. Sheng, and D. Y. Xing, "Chern number of thin films of the topological insulator Bi_2Se_3 ," *Phys. Rev. B* **82**, 165104 (2010).
- [12] Hai-Zhou Lu, An Zhao, and Shun-Qing Shen, "Quantum transport in magnetic topological insulator thin films," *Phys. Rev. Lett.* **111**, 146802 (2013).
- [13] Chui-Zhen Chen, Haiwen Liu, and X. C. Xie, "Effects of random domains on the zero Hall plateau in the quantum anomalous Hall effect," *Phys. Rev. Lett.* **122**, 026601 (2019).
- [14] Hai-Peng Sun, C. M. Wang, Song-Bo Zhang, Rui Chen, Yue Zhao, Chang Liu, Qihang Liu, Chaoyu Chen, Hai-Zhou Lu, and X. C. Xie, "Analytical solution for the surface states of the antiferromagnetic topological insulator MnBi_2Te_4 ," *Phys. Rev. B* **102**, 241406 (2020).
- [15] Chao-Xing Liu, Xiao-Liang Qi, Hai-Jun Zhang, Xi Dai, Zhong Fang, and Shou-Cheng Zhang, "Model Hamiltonian for topological insulators," *Phys. Rev. B* **82**, 045122 (2010).
- [16] S. Sajad Dabiri, Hosein Cheraghchi, and Ali Sadeghi, "Light-induced topological phases in thin films of magnetically doped topological insulators," *Phys. Rev. B* **103**, 205130 (2021).
- [17] S. Sajad Dabiri and Hosein Cheraghchi, "Engineering of topological phases in driven thin topological insulators: Structure inversion asymmetry effect," *Phys. Rev. B* **104**, 245121 (2021).
- [18] Hai-Peng Sun, Chang-An Li, Sang-Jun Choi, Song-Bo Zhang, Hai-Zhou Lu, and Björn Trauzettel, "Magnetic topological transistor exploiting layer-selective transport," *Phys. Rev. Res.* **5**, 013179 (2023).

- [19] Fang Qin, Rui Chen, and Hai-Zhou Lu, “Phase transitions in intrinsic magnetic topological insulator with high-frequency pumping,” *Journal of Physics: Condensed Matter* **34**, 225001 (2022).
- [20] Tongshuai Zhu, Huaiqiang Wang, and Haijun Zhang, “Floquet engineering of magnetic topological insulator MnBi_2Te_4 films,” *Phys. Rev. B* **107**, 085151 (2023).
- [21] Kai-Yu Yang, Yuan-Ming Lu, and Ying Ran, “Quantum hall effects in a weyl semimetal: Possible application in pyrochlore iridates,” *Phys. Rev. B* **84**, 075129 (2011).
- [22] Chui-Zhen Chen, Juntao Song, Hua Jiang, Qing-feng Sun, Ziqiang Wang, and X. C. Xie, “Disorder and metal-insulator transitions in weyl semimetals,” *Phys. Rev. Lett.* **115**, 246603 (2015).
- [23] Rui Chen, Dong-Hui Xu, and Bin Zhou, “Floquet topological insulator phase in a weyl semimetal thin film with disorder,” *Phys. Rev. B* **98**, 235159 (2018).
- [24] Rui Chen, Chui-Zhen Chen, Jin-Hua Sun, Bin Zhou, and Dong-Hui Xu, “Phase diagrams of weyl semimetals with competing intraorbital and interorbital disorders,” *Phys. Rev. B* **97**, 235109 (2018).
- [25] Xiao-Ping Li, Ke Deng, Botao Fu, Yongkai Li, Da-Shuai Ma, JunFeng Han, Jianhui Zhou, Shuyun Zhou, and Yugui Yao, “Type-III Weyl semimetals: $(\text{TaSe}_4)_2\text{I}$,” *Phys. Rev. B* **103**, L081402 (2021).
- [26] Rui Chen, Tianyu Liu, C. M. Wang, Hai-Zhou Lu, and X. C. Xie, “Field-Tunable One-Sided Higher-Order Topological Hinge States in Dirac Semimetals,” *Phys. Rev. Lett.* **127**, 066801 (2021).
- [27] Rui Chen, Hai-Peng Sun, Mingqiang Gu, Chun-Bo Hua, Qihang Liu, Hai-Zhou Lu, and XC Xie, “Layer Hall effect induced by hidden Berry curvature in antiferromagnetic insulators,” *National Science Review* **11**, nwac140 (2024).
- [28] Rui Chen, Hai-Peng Sun, and Bin Zhou, “Side-surface-mediated hybridization in axion insulators,” *Phys. Rev. B* **107**, 125304 (2023).
- [29] Rui Chen, Hai-Peng Sun, Bin Zhou, and Dong-Hui Xu, “Chiral edge state coupling theory of transport in quantum anomalous hall insulators,” *Sci. China Phys. Mech. Astron.* **66**, 287211 (2023).
- [30] Yi-Fan Zhao, Ruoxi Zhang, Ling-Jie Zhou, Ruobing Mei, Zi-Jie Yan, Moses H. W. Chan, Chao-Xing Liu, and Cui-Zu Chang, “Zero Magnetic Field Plateau Phase Transition in Higher Chern Number Quantum Anomalous Hall Insulators,” *Phys. Rev. Lett.* **128**, 216801 (2022).
- [31] Yuriko Baba, Mario Amado, Enrique Diez, Francisco Domínguez-Adame, and Rafael A. Molina, “Effect of external fields in high Chern number quantum anomalous Hall insulators,” *Phys. Rev. B* **106**, 245305 (2022).
- [32] Zeyu Li, Yulei Han, and Zhenhua Qiao, “Chern Number Tunable Quantum Anomalous Hall Effect in Monolayer Transitional Metal Oxides via Manipulating Magnetization Orientation,” *Phys. Rev. Lett.* **129**, 036801 (2022).
- [33] Shengshi Li, Xinyang Li, Weixiao Ji, Ping Li, Shishen Yan, and Changwen Zhang, “Quantum anomalous Hall effect with a high and tunable Chern number in monolayer NdN_2 ,” *Physical Chemistry Chemical Physics* **25**, 18275–18283 (2023).
- [34] Xiangang Wan, Ari M. Turner, Ashvin Vishwanath, and Sergey Y. Savrasov, “Topological semimetal and Fermi-arc surface states in the electronic structure of pyrochlore iridates,” *Phys. Rev. B* **83**, 205101 (2011).
- [35] Ching-Kit Chan, Patrick A. Lee, Kenneth S. Burch, Jung Hoon Han, and Ying Ran, “When Chiral Photons Meet Chiral Fermions: Photoinduced Anomalous Hall Effects in Weyl Semimetals,” *Phys. Rev. Lett.* **116**, 026805 (2016).
- [36] Binghai Yan and Claudia Felser, “Topological materials: Weyl semimetals,” *Annual Review of Condensed Matter Physics* **8**, 337–354 (2017).
- [37] Cheng Guo, Viktor S Asadchy, Bo Zhao, and Shanhui Fan, “Light control with Weyl semimetals,” *eLight* **3**, 2 (2023).
- [38] Hui Li, Hongtao He, Hai-Zhou Lu, Huachen Zhang, Hongchao Liu, Rong Ma, Zhiyong Fan, Shun-Qing Shen, and Jiannong Wang, “Negative magnetoresistance in Dirac semimetal Cd_3As_2 ,” *Nature communications* **7**, 10301 (2016).
- [39] Hai-Zhou Lu and Shun-Qing Shen, “Quantum transport in topological semimetals under magnetic fields,” *Frontiers of Physics* **12**, 1–18 (2017).
- [40] Holger Bech Nielsen and Masao Ninomiya, “Absence of neutrinos on a lattice:(i). proof by homotopy theory,” *Nuclear Physics B* **185**, 20–40 (1981).
- [41] Holger Bech Nielsen and Masao Ninomiya, “Absence of neutrinos on a lattice:(ii). intuitive topological proof,” *Nuclear Physics B* **193**, 173–194 (1981).
- [42] Yuehui Lu, Ningyuan Jia, Lin Su, Clai Owens, Gediminas Juzeliūnas, David I. Schuster, and Jonathan Simon, “Probing the Berry curvature and Fermi arcs of a Weyl circuit,” *Phys. Rev. B* **99**, 020302 (2019).
- [43] Ching Hua Lee, Amanda Sutrisno, Tobias Hofmann, Tobias Helbig, Yuhan Liu, Yee Sin Ang, Lay Kee Ang, Xiao Zhang, Martin Greiter, and Ronny Thomale, “Imaging nodal knots in momentum space through topolectrical circuits,” *Nature communications* **11**, 4385 (2020).
- [44] Tena Dubček, Colin J. Kennedy, Ling Lu, Wolfgang Ketterle, Marin Soljačić, and Hrvoje Buljan, “Weyl Points in Three-Dimensional Optical Lattices: Synthetic Magnetic Monopoles in Momentum Space,” *Phys. Rev. Lett.* **114**, 225301 (2015).
- [45] Sthitadhi Roy, Michael Kolodrubetz, Nathan Goldman, and Adolfo G Grushin, “Tunable axial gauge fields in engineered weyl semimetals: semiclassical analysis and optical lattice implementations,” *2D Materials* **5**, 024001 (2018).
- [46] Zong-Yao Wang, Xiang-Can Cheng, Bao-Zong Wang, Jin-Yi Zhang, Yue-Hui Lu, Chang-Rui Yi, Sen Niu, Youjin Deng, Xiong-Jun Liu, Shuai Chen, *et al.*, “Realization of an ideal Weyl semimetal band in a quantum gas with 3D spin-orbit coupling,” *Science* **372**, 271–276 (2021).
- [47] Yue-Hui Lu, Bao-Zong Wang, and Xiong-Jun Liu, “Ideal Weyl semimetal with 3D spin-orbit coupled ultracold quantum gas,” *Science Bulletin* **65**, 2080–2085 (2020).
- [48] Ling Lu, Zhiyu Wang, Dexin Ye, Lixin Ran, Liang Fu, John D Joannopoulos, and Marin Soljačić, “Experimental observation of weyl points,” *Science* **349**, 622–624 (2015).
- [49] Feng Li, Xueqin Huang, Jiuyang Lu, Jiahong Ma, and Zhengyou Liu, “Weyl points and fermi arcs in a chiral phononic crystal,” *Nature Physics* **14**, 30–34 (2018).
- [50] Meng Xiao, Wen-Jie Chen, Wen-Yu He, and Che Ting Chan, “Synthetic gauge flux and weyl points in acoustic systems,” *Nature Physics* **11**, 920–924 (2015).
- [51] Zhaoju Yang and Baile Zhang, “Acoustic Type-II Weyl Nodes from Stacking Dimerized Chains,” *Phys. Rev. Lett.* **117**, 224301 (2016).
- [52] Valerio Peri, Marc Serra-Garcia, Roni Ilan, and Se-

- bastian D Huber, “Axial-field-induced chiral channels in an acoustic weyl system,” *Nature Physics* **15**, 357–361 (2019).
- [53] Song-Bo Zhang, Xiaoxiong Liu, Md Shafayat Hossain, Jia-Xin Yin, M. Zahid Hasan, and Titus Neupert, “Emergent edge modes in shifted quasi-one-dimensional charge density waves,” *Phys. Rev. Lett.* **130**, 106203 (2023).
- [54] Zengle Huang, Hemian Yi, Lujin Min, Zhiqiang Mao, Cui-Zu Chang, and Weida Wu, “Absence of in-gap modes in charge density wave edge dislocations of the Weyl semimetal $(\text{TaSe}_4)_2\text{I}$,” *Phys. Rev. B* **104**, 205138 (2021).
- [55] Fang Qin, Shuai Li, Z. Z. Du, C. M. Wang, Wenqing Zhang, Dapeng Yu, Hai-Zhou Lu, and X. C. Xie, “Theory for the Charge-Density-Wave Mechanism of 3D Quantum Hall Effect,” *Phys. Rev. Lett.* **125**, 206601 (2020).
- [56] Supplemental Materials.
- [57] Takahiro Fukui, Yasuhiro Hatsugai, and Hiroshi Suzuki, “Chern numbers in discretized Brillouin zone: efficient method of computing (spin) Hall conductances,” *Journal of the Physical Society of Japan* **74**, 1674–1677 (2005).
- [58] M. M. Otrokov, I. P. Rusinov, M. Blanco-Rey, M. Hoffmann, A. Yu. Vyazovskaya, S. V. Eremeev, A. Ernst, P. M. Echenique, A. Arnau, and E. V. Chulkov, “Unique thickness-dependent properties of the van der Waals interlayer antiferromagnet MnBi_2Te_4 films,” *Phys. Rev. Lett.* **122**, 107202 (2019).
- [59] Anyuan Gao, Yu-Fei Liu, Chaowei Hu, Jian-Xiang Qiu, Christian Tzschaschel, Barun Ghosh, Sheng-Chin Ho, Damien Bérubé, Rui Chen, Haipeng Sun, *et al.*, “Layer Hall effect in a 2D topological axion antiferromagnet,” *Nature* **595**, 521–525 (2021).
- [60] Roger S. K. Mong, Andrew M. Essin, and Joel E. Moore, “Antiferromagnetic topological insulators,” *Phys. Rev. B* **81**, 245209 (2010).
- [61] Andrew M. Essin, Joel E. Moore, and David Vanderbilt, “Magnetoelectric polarizability and axion electrodynamics in crystalline insulators,” *Phys. Rev. Lett.* **102**, 146805 (2009).
- [62] Jing Wang, Biao Lian, Xiao-Liang Qi, and Shou-Cheng Zhang, “Quantized topological magnetoelectric effect of the zero-plateau quantum anomalous hall state,” *Phys. Rev. B* **92**, 081107 (2015).
- [63] Nicodemos Varnava and David Vanderbilt, “Surfaces of axion insulators,” *Phys. Rev. B* **98**, 245117 (2018).
- [64] Bo Fu, Zi-Ang Hu, and Shun-Qing Shen, “Bulk-hinge correspondence and three-dimensional quantum anomalous hall effect in second-order topological insulators,” *Phys. Rev. Res.* **3**, 033177 (2021).
- [65] H. M. Price, O. Zilberberg, T. Ozawa, I. Carusotto, and N. Goldman, “Four-Dimensional Quantum Hall Effect with Ultracold Atoms,” *Phys. Rev. Lett.* **115**, 195303 (2015).
- [66] Xiao Zhang, Youjian Chen, Yuzhu Wang, Yuhan Liu, Jun Yu Lin, Nai Chao Hu, Bochen Guan, and Ching Hua Lee, “Entangled four-dimensional multicomponent topological states from photonic crystal defects,” *Phys. Rev. B* **100**, 041110 (2019).
- [67] D. J. Thouless, M. Kohmoto, M. P. Nightingale, and M. den Nijs, “Quantized Hall conductance in a two-dimensional periodic potential,” *Phys. Rev. Lett.* **49**, 405 (1982).
- [68] Tian-Shi Xiong, Jiangbin Gong, and Jun-Hong An, “Towards large-Chern-number topological phases by periodic quenching,” *Phys. Rev. B* **93**, 184306 (2016).
- [69] Hui Liu, Tian-Shi Xiong, Wei Zhang, and Jun-Hong An, “Floquet engineering of exotic topological phases in systems of cold atoms,” *Phys. Rev. A* **100**, 023622 (2019).
- [70] Fangyang Zhan, Rui Chen, Zhen Ning, Da-Shuai Ma, Ziming Wang, Dong-Hui Xu, and Rui Wang, “Perspective: Floquet engineering topological states from effective models towards realistic materials,” *Quantum Frontiers* **3**, 21 (2024).
- [71] Fang Qin, Ching Hua Lee, and Rui Chen, “Light-induced phase crossovers in a quantum spin Hall system,” *Phys. Rev. B* **106**, 235405 (2022).
- [72] Fang Qin, Rui Chen, and Ching Hua Lee, “Light-enhanced nonlinear Hall effect,” *Communications Physics* **7**, 368 (2024).
- [73] S. Sajad Dabiri, Hosein Cheraghchi, and Ali Sadeghi, “Floquet states and optical conductivity of an irradiated two-dimensional topological insulator,” *Phys. Rev. B* **106**, 165423 (2022).
- [74] Hosein Cheraghchi and Zahra Askarpour, “Light-induced switch based on edge modes in irradiated thin topological insulators,” *Physica Scripta* **98**, 055917 (2023).
- [75] Anastasiia A. Pervishko, Dmitry Yudin, and Ivan A. Shelykh, “Impact of high-frequency pumping on anomalous finite-size effects in three-dimensional topological insulators,” *Phys. Rev. B* **97**, 075420 (2018).
- [76] Takashi Oka and Hideo Aoki, “Photovoltaic Hall effect in graphene,” *Phys. Rev. B* **79**, 081406 (2009).
- [77] H. L. Calvo, L. E. F. Foa Torres, P. M. Perez-Piskunow, C. A. Balseiro, and Gonzalo Usaj, “Floquet interface states in illuminated three-dimensional topological insulators,” *Phys. Rev. B* **91**, 241404 (2015).
- [78] Ranjani Seshadri and Diptiman Sen, “Engineering Floquet topological phases using elliptically polarized light,” *Phys. Rev. B* **106**, 245401 (2022).
- [79] Ranjani Seshadri, Anirban Dutta, and Diptiman Sen, “Generating a second-order topological insulator with multiple corner states by periodic driving,” *Phys. Rev. B* **100**, 115403 (2019).
- [80] Ranjani Seshadri, “Floquet topological phases on a honeycomb lattice using elliptically polarized light,” *Materials Research Express* **10**, 024002 (2023).
- [81] Ching Hua Lee, Wen Wei Ho, Bo Yang, Jiangbin Gong, and Zlatko Papić, “Floquet Mechanism for Non-Abelian Fractional Quantum Hall States,” *Phys. Rev. Lett.* **121**, 237401 (2018).
- [82] Wilhelm Magnus, “On the exponential solution of differential equations for a linear operator,” *Communications on pure and applied mathematics* **7**, 649 (1954).
- [83] Sergio Blanes, Fernando Casas, Jose-Angel Oteo, and José Ros, “The magnus expansion and some of its applications,” *Physics reports* **470**, 151 (2009).
- [84] Marin Bukov, Luca D’Alessio, and Anatoli Polkovnikov, “Universal high-frequency behavior of periodically driven systems: from dynamical stabilization to Floquet engineering,” *Advances in Physics* **64**, 139–226 (2015).
- [85] André Eckardt and Egidijus Anisimovas, “High-frequency approximation for periodically driven quantum systems from a Floquet-space perspective,” *New journal of physics* **17**, 093039 (2015).
- [86] Rui Chen, Bin Zhou, and Dong-Hui Xu, “Floquet Weyl semimetals in light-irradiated type-II and hybrid line-node semimetals,” *Phys. Rev. B* **97**, 155152 (2018).

- [87] Rui Chen, Dong-Hui Xu, and Bin Zhou, “Floquet topological insulator phase in a Weyl semimetal thin film with disorder,” *Phys. Rev. B* **98**, 235159 (2018).
- [88] Xiu-Li Du, Rui Chen, Rui Wang, and Dong-Hui Xu, “Weyl nodes with higher-order topology in an optically driven nodal-line semimetal,” *Phys. Rev. B* **105**, L081102 (2022).
- [89] Zi-Ming Wang, Rui Wang, Jin-Hua Sun, Ting-Yong Chen, and Dong-Hui Xu, “Floquet Weyl semimetal phases in light-irradiated higher-order topological Dirac semimetals,” *Phys. Rev. B* **107**, L121407 (2023).
- [90] Nico M Temme, *Special functions: An introduction to the classical functions of mathematical physics* (John Wiley & Sons, 1996).
- [91] Jia Ningyuan, Clai Owens, Ariel Sommer, David Schuster, and Jonathan Simon, “Time- and Site-Resolved Dynamics in a Topological Circuit,” *Phys. Rev. X* **5**, 021031 (2015).